JGR Solid Earth

RESEARCH ARTICLE
10.1029/2020JB020105

Benchmarking Component Analysis of Remanent Magnetization Curves With a Synthetic Mixture Series: Insight Into the Reliability of Unmixing Natural Samples

Kuang He[1,2,3], Xiangyu Zhao[4], Yongxin Pan[1,2,3,5], Xiang Zhao[6], Huafeng Qin[3,7], and Tongwei Zhang[1,2,3]

[1]Paleomagnetism and Geochronology Laboratory, Key Laboratory of Earth and Planetary Physics, Institute of Geology and Geophysics, Chinese Academy of Sciences, Beijing, China, [2]France-China Joint Laboratory for Evolution and Development of Magnetotactic Multicellular Organisms (LIA-MagMC), Chinese Academy of Sciences, Beijing, China, [3]Innovation Academy for Earth Science, Chinese Academy of Sciences, Beijing, China, [4]National Institute of Polar Research, Tokyo, Japan, [5]College of Earth and Planetary Sciences, University of Chinese Academy of Sciences, Beijing, China, [6]Research School of Earth Sciences, Australian National University, Canberra, Australian Capital Territory, Australia, [7]State Key Laboratory of Lithospheric Evolution, Institute of Geology and Geophysics, Chinese Academy of Sciences, Beijing, China

Key Points:
- Methods that unmix remanent magnetization curves individually and collectively are benchmarked using synthetic mixtures
- Limitations of both unmixing methods are comprehensively elaborated
- We demonstrate the two methods can be quantitatively combined to improve unmixing of natural samples

Correspondence to:
X. Zhao,
zhao.xiangyu@nipr.ac.jp

Citation:
He, K., Zhao, X., Pan, Y., Zhao, X., Qin, H., & Zhang, T. (2020). Benchmarking component analysis of remanent magnetization curves with a synthetic mixture series: Insight into the reliability of unmixing natural samples. *Journal of Geophysical Research: Solid Earth*, *125*, e2020JB020105. https://doi.org/10.1029/2020JB020105

Received 5 MAY 2020
Accepted 21 SEP 2020
Accepted article online 24 SEP 2020

Abstract Geological samples often contain several magnetic components associated with different geological processes. Component analysis of remanent magnetization curves has been widely applied to decompose convoluted information. However, the reliability of commonly used methods is poorly assessed as independent verification is rarely available. For this purpose, we designed an experiment using a series of mixtures of two endmembers to benchmark unmixing methods for isothermal remanent magnetization (IRM) acquisition curves. First-order reversal curves (FORC) diagrams were analyzed for comparison. It is demonstrated that the parametric method, which unmixes samples using specific probability distributions, may result in biased estimates. In contrast, an endmember-based IRM unmixing approach yielded better quantitative results, which are comparable to the results obtained by FORC analysis based on principle component analysis (FORC-PCA). We demonstrate that endmember-based methods are in principle more suitable for unmixing a collection of samples with common endmembers; however, the level of decomposition will vary depending on the difference between the true endmembers that are associated with distinctive processes and the empirical endmembers used for unmixing. When it is desired to further decompose endmembers, the parametric unmixing approach remains a valuable means of inferring their underlying components. We illustrate that the results obtained by endmember-based and parametric methods can be quantitatively combined to provide improved unmixing results at the level of parametric model distributions.

1. Introduction

As a widespread mineral group in natural environments, magnetic minerals often occur as mixtures of magnetic components of different origins that have distinct magnetic properties (Egli, 2004a; Roberts et al., 2006). Bulk magnetic parameters have long been used to preliminarily infer underlying components (e.g., Channell et al., 2013; King & Channell, 1991; Lascu et al., 2010; Liu et al., 2012; Lowrie, 1990; Moskowitz et al., 1993; Pan et al., 2005) or classify samples (Day et al., 1977; Dunlop, 2002; Roberts et al., 2018). Over the recent two decades, statistical analyses on a sequence of measurements, instead of bulk parameters, have achieved great popularity. In particular, isothermal remanent magnetization (IRM) curves have been one of the most deployed data for the analysis called IRM unmixing that can be done by parametric or nonparametric methods (see Heslop, 2015, for a comprehensive review). Both methods assume that an IRM curve as well as its first-order derivative, called the coercivity distribution or IRM gradient curve, is a linear combination of underlying components. The parametric method assumes the coercivity distribution of all components follows a specific mathematical probability distribution, called the model distribution or basis function. The components of a sample can be reconstructed by fitting a linear mixture model to IRM curves or corresponding coercivity distributions. Thus far, four model distributions have been proposed, which are the

lognormal distribution (Heslop et al., 2002; Kruiver et al., 2001; Robertson & France, 1994), the skewed generalized Gaussian (SGG) distribution (Egli, 2003), the skew normal distribution (Maxbauer et al., 2016), and the Burr-type XII distribution (Zhao et al., 2018). It is oftentimes not trivial to choose a model distribution for determining components. If the model distribution is different from that of underlying components, reconstruction may be biased (Egli, 2003; Zhao et al., 2018). Moreover, solutions of IRM unmixing are often nonunique, which is subject to measurement noise and the choice of initial guesses for parameters of individual components (Zhao et al., 2018). In order to decrease the uncertainty of IRM unmixing results, Egli (2003) highlighted the importance of quality control on measurements. Recently, Zhao et al. (2018) proposed an automated protocol for analysis on original IRM curves, rather than IRM gradient curves, to avoid amplification of measurement noise and to minimize the subjectivity involved in selecting initial guesses for parameters. As the parametric statistical method is often applied without explicit constraints from other samples, it is referred to as single-sample-based IRM (SS-IRM) unmixing in this study.

Heslop and Dillon (2007) proposes a nonparametric approach to decomposing IRM curves of a collection of IRM curves using nonnegative matrix factorization (NMF). This endmember modeling technique could unmix a dataset without any presumption of model distributions, avoiding the challenge in selecting optimal model distributions for SS-IRM unmixing. It has been demonstrated to be a powerful tool for samples with complicated properties (Dekkers, 2012; Fabian et al., 2016; Just et al., 2012). However, the endmember solution is not only inherently nonunique but also sensitive to the dataset under investigation (Weltje, 1997). If the extreme observations in datasets do not sufficiently approximate the corresponding true endmembers of a mixing system, the estimated endmembers may fail to represent the true endmembers (Heslop, 2015). In addition, this method does not differentiate components whose concentrations vary in proportion (Dekkers, 2012), meaning that the method cannot be used to identify underlying components of endmembers.

In addition to remanent magnetization curves, first-order reversal curve (FORC) diagrams have been widely applied to discern domain states of magnetic minerals (Pike et al., 1999; Roberts et al., 2000; Zhao et al., 2017) and to quantify noninteracting and/or weakly interacting single domain (SD) components (Egli et al., 2010). More recently, a statistical approach of FORC analysis based on the principle component analysis (FORC-PCA) (Harrison et al., 2018; Lascu et al., 2015) has been demonstrated to be a powerful unmixing method. As with the NMF approach of IRM unmixing, FORC-PCA analyzes samples collectively and does not require a priori knowledge on endmembers. Furthermore, the information on domain states of endmembers resulted from FORC-PCA may benefit associated interpretations (Roberts et al., 2018). Notwithstanding, FORC measurements are way more time consuming than IRM measurements, even with an efficient protocol using nonlinear field increments (Zhao et al., 2015), which prevents it from becoming a routine option for unmixing a large number of samples.

Common to all unmixing approaches, it remains difficult to verify whether the results are reliable as it is impractical to ground-truth the results for natural samples. This fact deeply concerns numerous applications that are based on component analysis to infer related geological or paleoenvironmental information. Among these applications, biogenic magnetic particles have become an increasingly popular target; however, great challenges persist for obtaining adequate quantification. As inorganic remnants of widespread magnetotactic bacteria (MTB) (e.g., Frankel & Blakemore, 1989; Lin et al., 2014), magnetite magnetofossils have been considered as useful tracers for paleoclimate changes given the activities of MTB in geochemical cycling (Chen et al., 2014; Larrasoaña et al., 2012; Lin et al., 2017; Roberts et al., 2011) and paleomagnetic recorders (Paterson et al., 2013; Zhao et al., 2016). In natural samples, however, they are often mixed with abiotic magnetite that usually have considerable overlapping coercivity distributions. It has been demonstrated by numerical examples that unmixing results of such cases are highly prone to bias (Zhao et al., 2018).

In this study, we evaluate the performance of IRM unmixing and FORC-PCA techniques on synthetic mixture samples consisting of two endmembers with reasonable overlapping coercivity distributions, which are cultivated magnetotactic bacteria (*Magnetospirillum gryphiswaldense* strain MSR-1) and andesite powders. The reconstructed components, including their concentrations and magnetic properties, are benchmarked to evaluate the effectiveness and reliability of the investigated methods. A straightforward approach of endmember-based IRM (EM-IRM) unmixing is developed to analyze the IRM curves of the mixture

samples, which generates improved results that are comparable to the estimates by FORC-PCA. Furthermore, EM-IRM unmixing is used to elaborate the connection between SS-IRM unmixing and general endmember-based methods, for example, NMF and FORC-PCA. We demonstrate that the two types of methods can be combined to better unmix natural samples.

2. Materials and Methods

2.1. Sample Preparation

The freeze-dried whole cells of *Magnetospirillum gryphiswaldense* strain MSR-1 were used as a biogenic endmember. The MSR-1 were cultivated following the protocol by Zhang and Pan (2018). The collected cells were spun for 40 h at 30°C in a shaker with a rotating speed of 100 rpm and then dried with a freeze dryer. An andesite, sampled from the Tiaojishan Formation in the Chengde area, China (Pei et al., 2011), was the other endmember as an analogue of detrital magnetic fractions in natural samples that have a broad range of coercivity. A total of seven samples were prepared for magnetic measurements, including the two endmembers (andesite and MSR-1) plus five mixture samples with designated mixing ratios, that is, Mix-A to E (Table 1). The samples were loaded in nonmagnetic capsules and stuffed with cotton wool to prevent powders from vibration during measurements.

To prepare samples for transmission electron microscopy (TEM) observation, freeze-dried MSR-1 samples were dissolved with distilled water and transferred to the surface of a carbon-coated copper grid. Redundant solution was removed using filter paper while the solution was drying in air. Andesite powders were added into a 50-ml centrifuge tube with distilled water. After the sample was homogenized by shaking, we used a magnet to extract magnetic particles out of the tube, and the magnetic extracts were transferred with a pipette to a double folding copper grid. Afterwards, the sample was air-dried.

2.2. TEM Observation of Magnetic Minerals

TEM observation was performed on a total of 471 MSR-1 magnetosomes and 43 particles magnetically extracted from andesite powders, respectively, to inspect the morphology and element using a high-resolution transmission electron microscopy (HRTEM, JEOL JEM2100) with energy dispersive X-ray spectroscopy (EDXS) at an accelerating voltage of 200 kV. Selected-area electron diffraction (SAED) patterns were recorded on magnetic extracts from andesite powders. The grain size of magnetosomes and magnetic particles was determined from TEM images using Gatan Digital Micrograph software.

2.3. Magnetic Measurements

Magnetic measurements, including hysteresis loops, IRM acquisition curves, backfield curves, and FORCs, were measured on a vibrating sample magnetometer (VSM, Princeton MicroMag 3900). Hysteresis loops were measured with field increments of 4 mT, ranging between maximum fields of ±500 mT with an averaging time of 1 s in order to improve the signal to noise ratio for samples with low saturation magnetization (M_s). IRM acquisition curves were obtained with logarithmic increments to a maximum field of 1 T. Single-axis demagnetization of samples was preformed prior to IRM acquisition. Backfield curves were measured following IRM measurements using identical parameters. FORCs were measured with an increment of 2.2 mT field in the range from −100 to 100 mT for B_u and from 0 to 100 mT for B_c, resulting in 150 curves for each sample.

2.4. Data Analyses

IRM curves were analyzed using both SS-IRM and EM-IRM unmixing. For SS-IRM unmixing, the lognormal distribution (Kruiver et al., 2001) and the Burr-type XII distribution (Zhao et al., 2018) were used as the model distributions. For EM-IRM unmixing, model distributions used in SS-IRM unmixing are replaced by customized model distributions that best fit the preselected endmembers. All IRM unmixing was performed on normalized acquisition curves, rather than their gradient curves in order to avoid amplification of measurement noise upon calculating derivatives (Zhao et al., 2018).

For SS-IRM unmixing, the model is expressed as

Table 1
Magnetic Parameters for Samples and Reconstructed Proportions for the MSR-1 Endmember

Sample ID	MSR-1 (wt.%)	Bulk parameters[a] M_s mAm^2/kg	M_{rs} mAm^2/kg	B_c mT	B_{cr} mT	IRM unmixing components	Contribution of MSR-1 endmember to bulk parameters: Expected M_s/M_{s_bulk}	Expected M_{rs}/M_{rs_bulk}	Reconstructed EM-IRM	Reconstructed FORC-PCA
andesite	0	703.09	105.70	10.55	28.15	4 *LN*[b]	0%	0%	0.30%	0.28%
MSR-1	100	87.93	26.90	5.83	11.62	2 *Burr*[c]	100%	100%	98.10%	99.70%
Mix-A	13.7	583.56	86.16	9.52	26.53	4 *LN*	1.95%	3.88%	8.67%	3.52%
Mix-B	31.4	445.71	65.50	8.43	24.89	4 *LN*	5.42%	10.44%	4.39%	7.40%
Mix-C	52.9	412.86	69.43	8.10	20.68	4 *LN*	12.30%	22.20%	26.15%	18.96%
Mix-D	61.3	339.78	57.20	7.52	20.74	4 *LN*	16.53%	28.72%	21.51%	19.77%
Mix-E	92.5	151.25	40.88	6.58	12.93	3 *LN*	60.67%	75.84%	79.95%	68.60%

[a]Bulk parameters are determined after slope correction following the protocol by Paterson et al. (2018). [b]*LN* stands for lognormal components. [c]*Burr* stands for Burr-type XII components.

$$M^*(B) = \frac{M(B)}{M_{rs}} = \sum_{i=1}^{n} c_i M_i(B; \boldsymbol{\Theta}_i) + \varepsilon(B), \quad (1)$$

where $M^*(B)$ is the IRM at field B normalized by the remanence magnetization (M_{rs}), $M_i(B; \boldsymbol{\Theta}_i)$ is the model distribution of the ith component with c_i and $\boldsymbol{\Theta}_i$ being the concentration and model parameters, respectively, and $\varepsilon(B)$ is the residual. For the lognormal distribution, $\boldsymbol{\Theta}_i$ includes two parameters, which are the scale and dispersion parameters. For the Burr-type XII distribution, $\boldsymbol{\Theta}_i$ includes one scale parameter and two shape parameters. To minimize uncertainty and subjectivity associated with the method, IRM curves were processed following the protocol suggested by Zhao et al. (2018) with minor modification. The protocol frees users from choosing initial guesses for related parameters, and the optimal model distribution and number of components were determined using the Akaike Information Criterion (AIC) (Akaike, 1998; Burnham & Anderson, 2002).

For each sample, the optimal component number and model distribution were firstly determined from multiple pilot runs ($n > 10$). In each run, 80% of data was resampled for IRM unmixing to randomize the impact of measurement noise on analysis. An optimization step followed pilot runs to estimate the uncertainty of fitting. Specifically, the optimal coercivity parameter for each component, which is the scale parameter for the lognormal and Burr-type XII distributions (Zhao et al., 2018), that results in minimum AIC was selected as the initial guess ($\widehat{B}_{ini}$) for optimization steps. The bounds for the coercivity parameter were then constrained within the range of $\widehat{B}_{ini} \pm 15\%\ \widehat{B}_{ini}$. Multiple optimizing runs ($n = 30$) were performed on resampled datasets (80% of original data) to obtain final best-fits as well as uncertainty estimates.

For a set of samples that have common backgrounds, such as geographical vicinity, common provenance, and similar geological processes, endmembers can often be selected to account for the variation in certain properties (e.g., coercivity) of all samples. This is equivalent to the following equation:

$$M^*(B) = \frac{M(B)}{M_{rs}} = \sum_{i=1}^{n} c_i M_i^c(B) + \varepsilon(B), \quad (2)$$

where $M_i^c(B)$ is the customized model distribution for the ith of a total of n endmembers. The critical difference from Equation 1 is that $M_i^c(B)$ does not have unknown parameters, which makes the model a linear function of c_i. Therefore, Equation 2 is a linear unmixing problem where information on endmembers is known (Weltje, 1997). For the mixtures used in this study, $M_i^c(B)$ corresponds to the MSR-1 and andesite powder endmembers and is modeled using Equation 1 whereby measurement noise is also minimized. FORCs were processed with the FORCinel package (Harrison & Feinberg, 2008) to extract the biogenic component and FORC-PCA (Harrison et al., 2018; Lascu et al., 2015) to unmix MSR-1 magnetosomes and magnetic minerals of andesites.

3. Results

3.1. Morphology and Grain Size Distribution of Magnetic Minerals

The MSR-1 magnetosomes generally have isotropic morphology. We find that extracted magnetosomes have several configurations, including long chains, bent or broken chains, and collapsed fragments (Figures 1a–1c), suggesting that some membranes of MSR-1 were broken upon preparation. The grain size of MSR-1's magnetosomes follows a Gaussian distribution with a mean of 29.2 nm and a standard deviation of 5.0 nm (Figure 1d).

The magnetic extracts of andesite powders show irregular shapes and large grain size with the length ranging from ~74 nm to 1.5 μm (See Figures 2a and 2d). According to EDXS analysis and SAED results, the majority of the magnetic extracts is magnetite (Figures 2b and 2c) with minor amount of hematite (See Figures 2e and 2f).

3.2. Magnetic Results

3.2.1. Hysteresis Loops and IRM Acquisition Curves

Hysteresis loops were measured to manifest the bulk rock magnetic properties of the samples under investigation (Figure 3a). Related hysteresis parameters are listed in Table 1, where the values of M_s, M_{rs}, and coercivity (B_c) are determined after slope corrections following the protocol by Paterson et al. (2018). The mass-specific M_s of andesite powders is 703.09 mAm^2/kg while that of dried MSR-1 whole cells is 87.93 mAm^2/kg. The grain size of MSR-1 magnetosomes lies within the range for SP and SD magnetite, and accordingly, the hysteresis loop is slightly wasp-waisted (Figure 3b) with the ratio of saturation remanence to saturation magnetization, M_{rs}/M_s, of ~0.31, which is lower than that of noninteracting uniaxial SD particles. The hysteresis loop of andesite powders is distinctive (Figure 3b) with $M_{rs}/M_s \approx 0.15$, indicating the magnetic grain size of the andesite endmember is coarser than that of the MSR-1 endmember. The shape of hysteresis loops changes accordingly with the mixing ratio (Figure 3b). The IRM acquisition curve of the MSR-1 endmember saturates more easily than that of the andesite powder (Figure 3c), which manifests the difference in their coercivity distributions. Both the mass specific M_{rs} and median coercivity of mixture samples decreases as the MSR-1 fraction increases.

Assuming the magnetization of the endmembers used in mixtures is identical, the expected bulk M_{rs} (or M_s) for the mixtures is linearly dependent on the mass fractions of the endmembers as indicated by the dotted line in Figure 3d. The measured values of bulk M_s and M_{rs} of the mixtures are in agreement with the expected trend with slight deviations, indicating that the magnetic properties of the endmembers added to mixture samples are not perfectly homogeneous. Note that the contributions of the endmembers to the bulk magnetization parameters of the mixtures, for example, M_{rs_bio}/M_{rs_bulk}, is a nonlinear function of the mass fraction since the mass-specific magnetization parameters are not equal for the two endmembers (see the inset of Figure 3d).

3.2.2. SS-IRM Unmixing

The IRM curves were automatically fitted using two model distributions, that is, the lognormal and Burr-type XII distributions and the solutions that result in minimal AIC estimators were chosen as the best fit. The optimal model distribution and component number are listed in Table 1. As shown in Figures 4a and 4g, the MSR-1 and andesite endmembers are best fitted with two Burr and four lognormal components, respectively. The mixture samples, therefore, can be viewed as mixtures of four lognormal components and two Burr components. The optimal numbers of components for the mixtures are, however, fewer than the number of components of the two endmembers combined (Table 1), implying that the reconstructed components deviate from the six components of the endmembers to some degree. The unmixing results are discussed below from the perspectives of shape and concentration, respectively.

In order to link the components reconstructed from the mixtures to that reconstructed from the endmembers, the coercivity distribution of every component is compared after normalization whereby the area under each curve is equal to one (Figure 4h). It is clear that the major component of the andesite endmember (AD-cp3, shown as the thick green curve) corresponds to Mix-cp3 of the mixtures (light green curves), except for sample Mix-E whose Mix-cp3 is more similar to AD-cp2 (thick orange curve). The high coercivity component of the andesite endmember (AD-cp4, thick red curve) and the major component of the MSR-1 endmember (MSR-cp2, dashed orange curve) correspond to Mix-cp4 (light red curves) and Mix-cp2

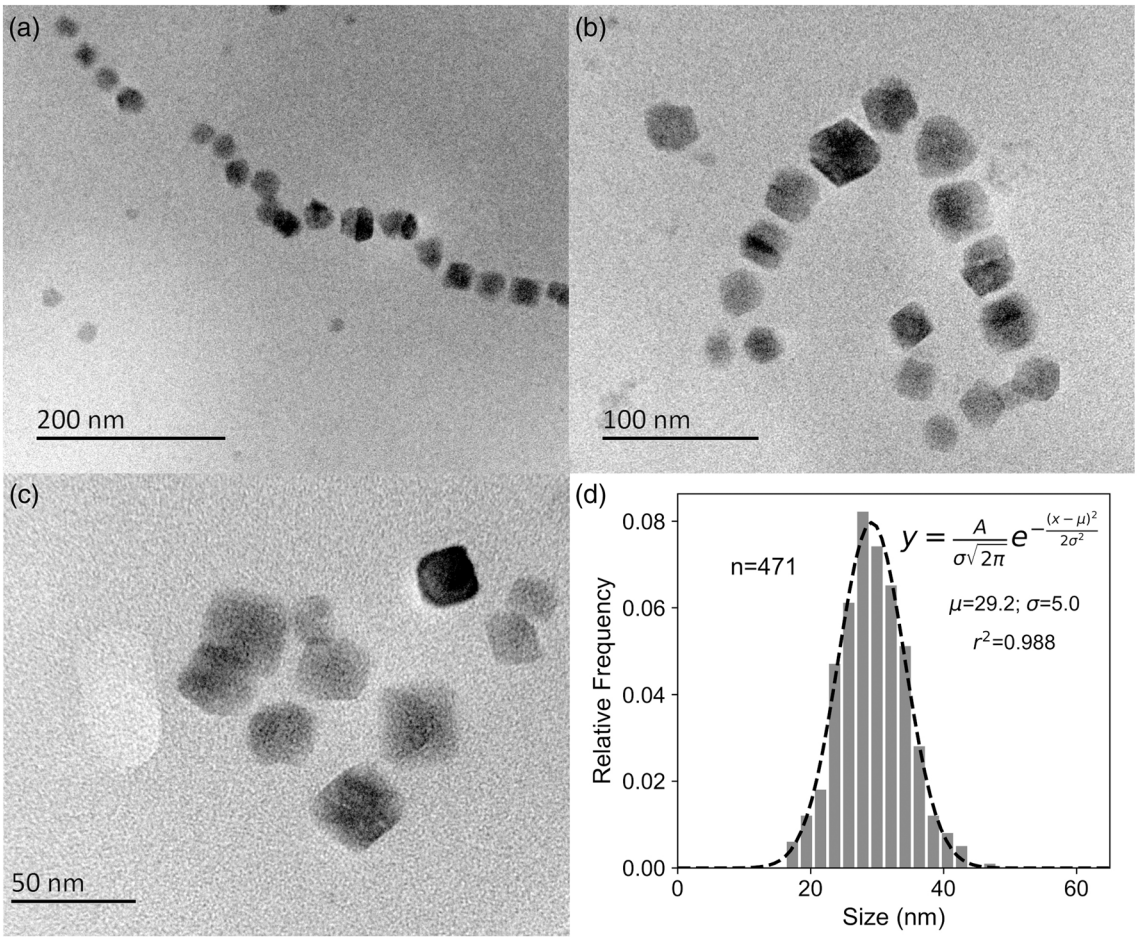

Figure 1. TEM images of (a–c) MSR-1 magnetosomes morphology and (d) grain size distribution.

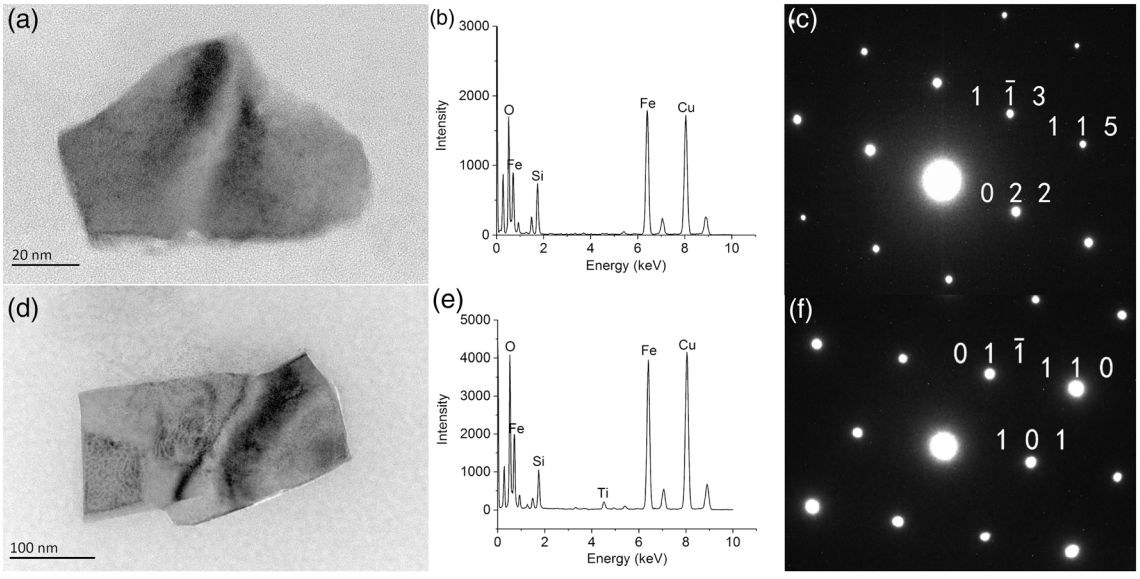

Figure 2. TEM analyses of magnetic extracts from andesite powers. (a) and (d) TEM images of magnetic extracts; (b) and (e) EDXS results of magnetic minerals shown in (a) and (d), respectively; (c) and (f) SAED of particles shown in (a) and (d), respectively.

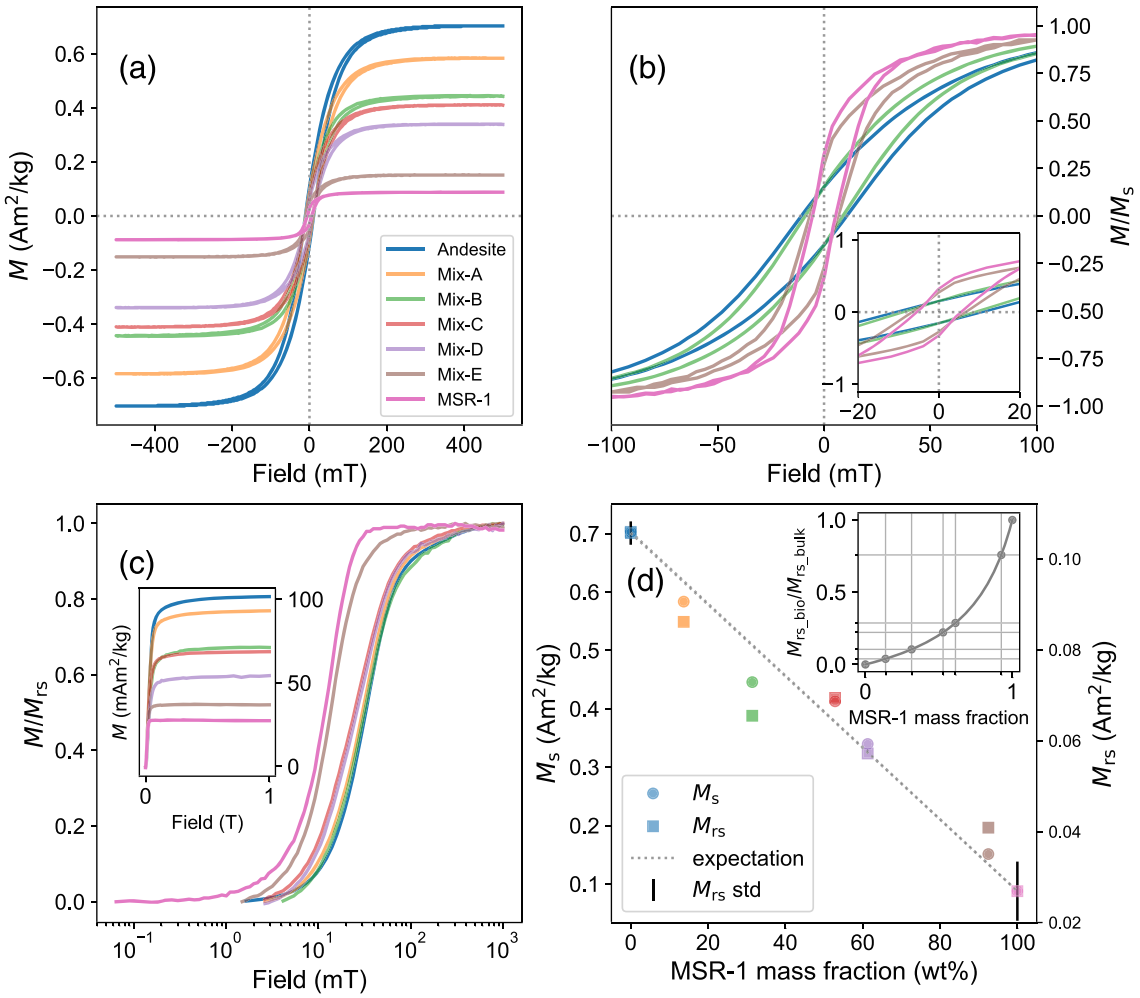

Figure 3. Hysteresis loops and IRM acquisition curves. (a) Mass normalized hysteresis loops of the endmembers and mixtures; (b) examples of hysteresis loops normalized by M_{rs}; (c) IRM acquisition curves normalized by M_{rs} and mass (inset), respectively; (d) measured M_{rs} (squares) and M_s (circles) of mixtures in relation to the mass fraction of the MSR-1 endmember. The standard deviations of M_{rs} of both endmembers are shown. The deviations of M_s are not shown because their amplitudes are similar to the size of the symbols, which makes it hard to be discerned. The expected trend is indicated by the dotted gray line. The inset shows the expected relationship between MSR-1 mass fraction and the contribution of the MSR-1 endmember to the bulk M_{rs} of mixtures. The color code is the same for all plots.

(light orange curves), respectively. Therefore, Mix-cp2, cp3, and cp4 can be interpreted as MSR-cp2, AD-cp3, and AD-cp4, respectively. In contrast, the minor components of the endmembers (AD-cp1 is shown as the thick blue curve and MSR-cp1 shown as the dashed blue curve) are not faithfully resolved from the mixture samples. For example, the reconstructed minor component of the mixture samples (Mix-cp1, light blue curves) apparently varies between AD-cp1 and MSR-cp1.

If the unmixing results were reliable, the concentrations of the reconstructed major components should match with their expected values closely, which is indicated by the 1:1 line in Figure 4i. However, the results are significantly greater than the expectation, especially for MSR-cp2 and AD-cp3. Notice that AD-cp2, which overlaps with both MSR-cp2 and AD-cp3, was missing from reconstruction (Figure 4h). It suggests that AD-cp2 was divided into Mix-cp2 and -cp3, rather than being identified as an individual component, which can account for the overestimates. AD-cp4 is much better quantified (see Figures 4h and 4i), except for sample Mix-E (92.5 wt% of MSR-1, Figure 4f) probably because of the marginal contribution of AD-cp4 to its bulk M_{rs} (which is expected to be only ~2.6%).

3.2.3. EM-IRM Unmixing

Figure 5 shows the results using EM-IRM unmixing with andesite and MSR-1 as the endmembers. For comparison, the expected data are shown (thick orange curves) along with measured data (dots), which are

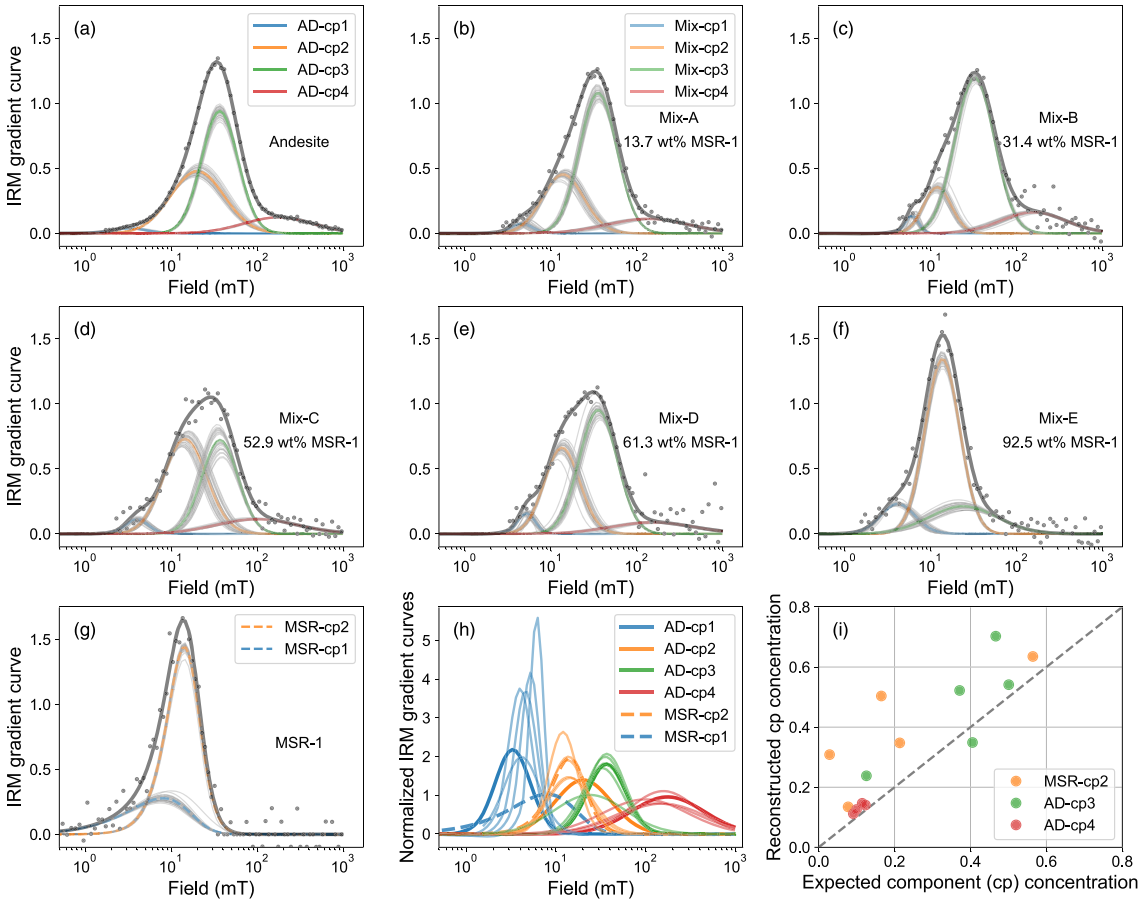

Figure 4. Results of SS-IRM unmixing. (a) The IRM gradient curve (dots) of the andesite endmember. SS-IRM unmixing is performed on the IRM acquisition curve using the automatic protocol by Zhao et al. (2018) to avoid amplification of measurement noise. The optimal components (AD-cps, color lines) reconstructed by SS-IRM unmixing are shown with thin gray lines indicating uncertainties; (b–f) four lognormal components optimally fit all mixtures except for (f); (g) the MSR-1 endmember is optimally fitted with two Burr-type XII components; (h) normalized coercivity distributions of all optimal components shown in (a–g). Note that components with similar coercivity range are shown in same or similar colors, which facilitate visualization and interpretation. Thick solid lines correspond to AD-cps in (a), thick dashed lines correspond to MSR-cps in (g), and the lines in light colors correspond to Mix-cps in (b–f); (i) the concentrations of the reconstructed components from mixtures versus their expected values based on the major components reconstructed from the endmembers (MSR-cp2 and AD-cp3, 4).

calculated by assuming that the andesite and MSR-1 fractions added in the mixtures have homogeneous magnetic properties. The measured data are overall close to the expected data, indicating that the assumption is valid. The best-fits of the mixtures by EM-IRM unmixing (thick black curves) are also close to the expected data with minor differences, and the reconstructed endmembers (solid green and red curves) are in accordance with the expected endmembers (dashed green and red curves) with acceptable biases. Overall, the estimated concentrations of the endmembers in the mixture samples are much improved compared to the results obtained by SS-IRM unmixing, as evidenced by the fact that estimates closely follow the values calculated based on the endmembers and their mixing ratios (Figure 5f).

3.2.4. FORC Diagrams and FORC-PCA

The FORC diagram of the andesite endmember is characterized by funnel-shaped contours that are asymmetric about the B_c axis (i.e., $B_u = 0$) and a narrow central ridge along the B_c axis, indicating existence of vortex and SD states (Figure 6a). For the MSR-1 endmember, the FORC diagram (Figure 6f) presents a central ridge and negatively magnetized region that are characteristic for weakly interacting SD particles (Egli et al., 2010; Newell, 2005; Zhao et al., 2017). For the mixtures, the FORC diagrams (Figures 6b–6e) are apparently responsive to the change in the mixing ratio of the endmembers.

For FORC-PCA, one principle component (PC) could describe more than 90% of the data variablity; the PC scores are plotted in Figure 6g. The MSR-1 magnetosomes and the andesite powder were used as two

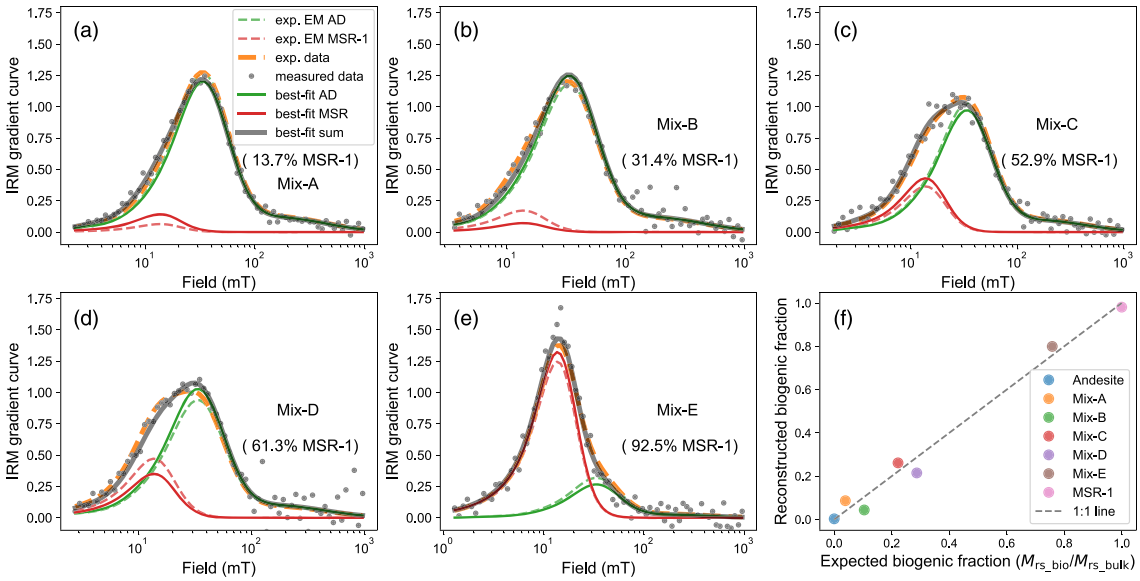

Figure 5. EM-IRM unmixing of mixtures. (a–e) Measured data (dots) of each mixture sample are compared against their respective expected data (orange dashed curves) which is calculated by assuming the magnetic properties of the endmembers (dashed green and red curves) added in the mixtures are homogeneous. Reconstructed endmembers using EM-IRM unmixing and their sums are shown in colored and black solid curves, respectively; (f) reconstructed contribution of the MSR-1 endmember in relation to the expected contribution of the biogenic endmember to bulk M_{rs}. The gray dashed line indicates the expected trend.

endmembers. The reconstructed contributions of the MSR-1 fraction in the mixture samples approximate to the expected values of M_{rs_bio}/M_{rs_bulk} (Figure 6h and Table 1). Note that the estimated contribution is significantly different from the expected values of M_{s_bio}/M_{s_bulk} (Table 1) in this case, which is because FORC signal is dominated by irreversible remanent magnetization in the range covered by our measurements (up to 100 mT) (Zhao et al., 2017) and has limited contribution from the reversible magnetization which is hard to be fully recovered during FORC reconstruction.

4. Discussion

As independent quantification methods for magnetic components are unavailable for most studies, it remains poorly known whether component analysis of remanent magnetization curves can reliably reconstruct the underlying components of studied samples. Two major concerns are (1) whether the reconstructed components can qualitatively represent that of the true components and (2) whether the estimated concentrations of components are reliable. In this part, we will elaborate these issues based on the ground-truth data following the discussion of magnetic property of MSR-1 magnetosomes and andesite powders and their eligibility as endmembers.

4.1. Validity of MSR-1 Magnetosomes and Andesite Powders as Endmembers

Over the past two decades, magnetofossils have been reported to be widespread in sediments, facilitated by FORC diagrams (e.g., Egli et al., 2010; Larrasoaña et al., 2012; Roberts et al., 2012) and unmixing of remanent magnetization curves (Egli, 2003, 2004a, 2004b; Usui et al., 2017). Given the variable physical property of wild-type MTB magnetosomes (e.g., Li et al., 2010; Mao et al., 2014; Pan et al., 2005), it is difficult to choose a "representative" wildtype biogenic endmember from natural samples. For a practical reason, we selected cultured MTB in order to make sure that the biogenic magnetite added to the synthetic samples has reproducible magnetic properties. The grain size of the MSR-1 magnetosome used in this study ranges from 16 to 48 nm in length, which follows a Gaussian distribution (Figure 1). There is a ~37% of particles with grain size between 25 and 30 nm, which is the size threshold from superparamagnetic (SP) to SD behavior for equidimensional magnetite (Dunlop, 1973; Dunlop & Bina, 1977; McNab et al., 1968). The grain size distribution is consistent with its wasp-waisted hysteresis loop (Tauxe et al., 1996) and the low coercivity distribution as seen on the FORC diagram and IRM acquisition curve. It is noticed that coercivity distribution of the MSR-1 endmember is significantly left-skewed, rather than being symmetric (Egli, 2003). The coercivity

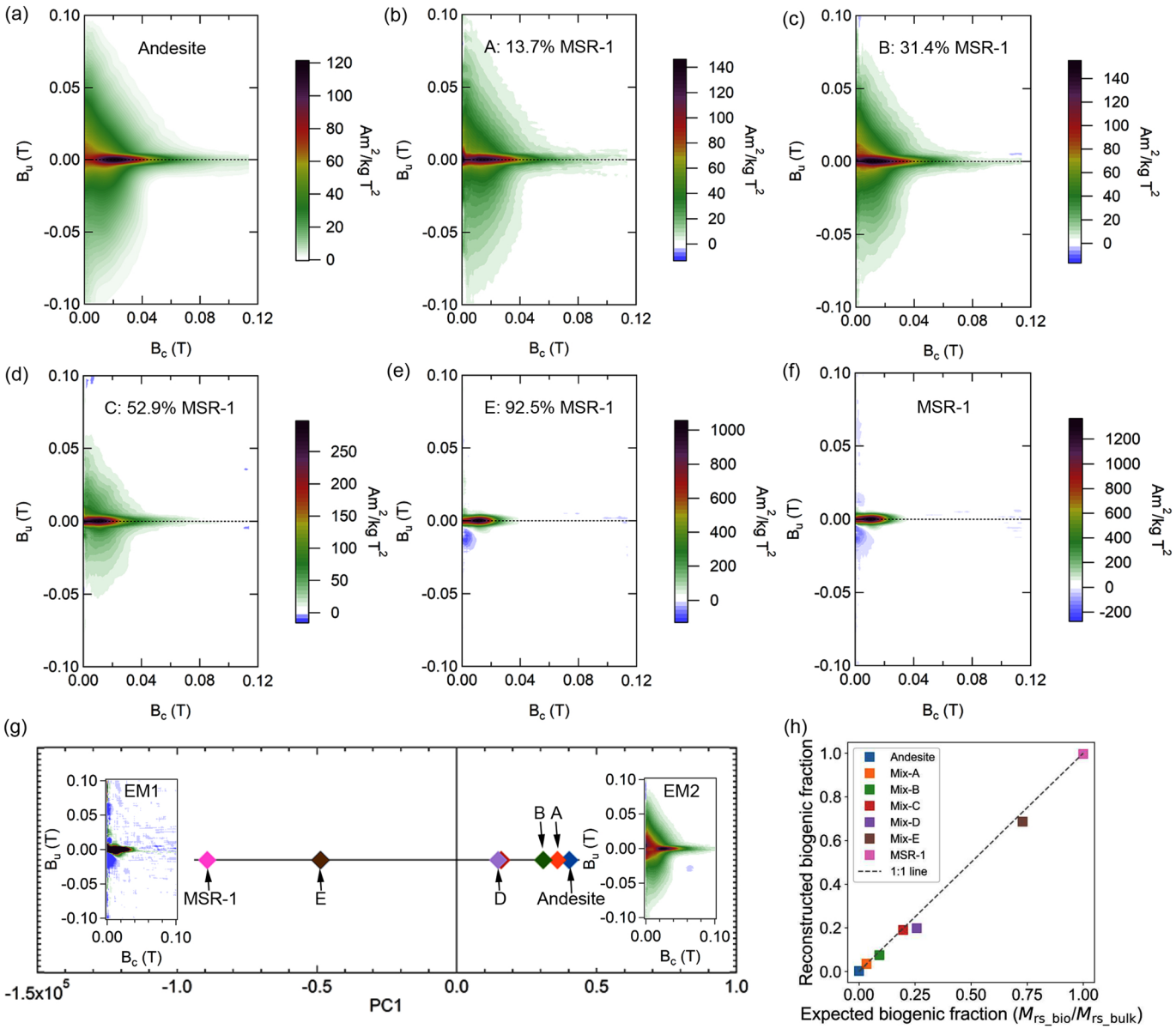

Figure 6. FORC diagrams and FORC-PCA results. (a–f) FORC diagrams of all samples; (g) reconstructed FORC diagrams of endmembers and the score of PC1; (h) reconstructed biogenic contributions vs. expected contributions of the MSR-1 endmember to bulk M_{rs}.

distribution of the MSR-1 could be fitted with two Burr components (MSR-cp1 and MSR-cp2) in which MSR-cp2 is nearly symmetric (Figure 4g). The asymmetric shape may be attributed to smaller coercivity of particles around the SP/SD boundary and/or interaction of collapsed chains or randomly aligned assemblages. Therefore, it demonstrates the coercivity distribution of a biogenic component could be inherently asymmetric, even it has symmetric grain size distribution.

The andesite powder presents distinct magnetic properties with respect to that of the biogenic endmember. The coercivity distribution of the andesite powder is relative complex, which requires four lognormal distributions to fit (Figure 4a). AD-cp1 and AD-cp2 overlap heavily with the MSR-1 endmember. But a considerable fraction of the andesite powder, accounting for >50% of its M_{rs}, distributes above 30 mT where the MSR-1 endmember almost saturates. In particular, AD-cp4 that accounts for ~13% of its M_{rs} (Figures 4a and 4h) hardly overlaps with the MSR-1 endmember. Based on its high coercivity and SAED result, AD-cp4 probably corresponds to hematite.

Overall, the magnetic properties of the andesite and MSR-1 endmembers exhibit realistic complexity for testing IRM unmixing. The coercivity distributions of their underlying components are moderately overlapping, which is relevant to a majority of cases of natural samples reported in literature (e.g., Egli, 2003, 2004a).

4.2. Limitations of SS-IRM Unmixing

A critical assumption of SS-IRM unmixing is that the coercivity distribution of a component can be described by a specific mathematical probability distribution. However, natural magnetic endmembers that represent distinct geological processes may inherently consist of multiple components such that their coercivity distributions are more complex than a single model distribution could describe, as demonstrated by the andesite endmembers used in this study (Figures 4a and 4g). Consequently, the number of components used for unmixing may be greater than that of actual components. When taking measurement noise and the inherent uncertainty of nonlinear optimization into consideration (Zhao et al., 2018), it means that reliable reconstruction becomes more challenging as the number of actual components increases, despite that given data can be closely fitted. Our results demonstrate two scenarios where SS-IRM unmixing may fail.

Firstly, it is difficult to faithfully reconstruct highly overlapping components. The reconstructed major components (Mix-cp2–4) were adequate in terms of shape as evidenced by the impressive consistency in their normalized coercivity distributions (Figure 4h). However, it turned out that Mix-cp2 and Mix-cp3 overestimate MSR-cp2 and AD-cp3, respectively (Figure 4i), which is probably owing to the interference of another overlapping component (AD-cp2). In contrast, the putative hematite component (AD-cp4) is better reconstructed from four out of the five mixtures (see Figures 4h and 4i), though the contribution of AD-cp4 to the bulk M_{rs} is much less than AD-cp3. The results strongly suggest that the distinctiveness in coercivity distributions of underlying components is crucial for achieving a faithful result using SS-IRM unmixing.

Secondly, reconstructed minor components can be suspicious, as evidenced by the heavily biased reconstruction of MSR-cp1 and AD-cp1. Minor components have marginal contributions to bulk M_{rs}; hence, they are highly sensitive to measurement noise and selection of component parameters. In practice, one should be cautious when interpreting minor components.

As stated above, SS-IRM unmixing may not be able to reliably decompose samples consisting of components with significantly overlapping coercivity distributions. Therefore, interpretations should be made cautiously for samples with complicated coercivity distributions (e.g., those require >3 overlapping components to fit). Furthermore, it is worth clarifying that the model distribution used by SS-IRM unmixing is more of a mathematical concept than a physical description (Zhao et al., 2018). Magnetic minerals formed under the same mechanism may be equivalent to multiple components of a given model distribution, such as the andesite endmember used in this study. A single component reconstructed by IRM unmixing may represent incomplete information about or even irrelevant to a geological process.

4.3. Limitations of EM-IRM Unmixing

The EM-IRM unmixing approach (Equation 2) can be expressed in a matrix form:

$$D = WM + E, \tag{3}$$

where D is the data matrix with each row being an IRM curve, M is the matrix of endmembers, W is the matrix of mixing proportions of endmembers for corresponding samples, and E is the residual. If both W and M are treated as unknowns, EM-IRM unmixing is essentially the same as the NMF approach of IRM unmixing (Heslop & Dillon, 2007). On the other hand, M can also be set by users based on empirical or statistical evidences as with FORC-PCA (Lascu et al., 2015). Therefore, the limitations of EM-IRM unmixing in the following discussion also provide insights into the limitations of existing endmember-based unmixing methods, which is the choice of basis for decomposition.

As illustrated by the previous example, using endmembers could greatly simplify the unmixing problem and improve the results. Nevertheless, it is crucial to realize that the level of unmixing is sensitive to the choice of endmembers. True endmembers (M_{true}) that represent distinct processes or sources are optimal for unmixing. When M_{true} can be defined by a priori knowledge or reconstructed from datasets, resulting W_{true} represents the mixing proportions of the true endmembers. However, natural samples may rarely consist of true endmembers, meaning observed data may vary in a subspace of the full mixing space defined by true

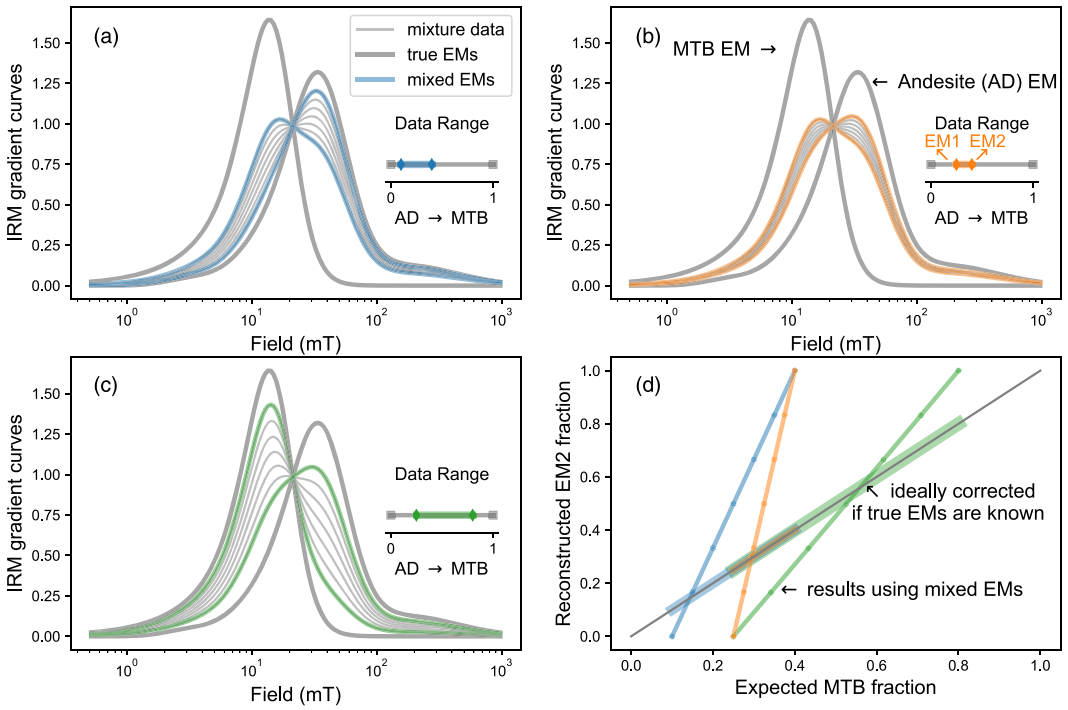

Figure 7. Effects of endmembers on EM-IRM unmixing. (a–c) Numerical synthetic IRM curves with the MSR-1 and andesite endmembers being the true endmembers (thick gray curves). EM-IRM unmixing was performed on datasets where the IRM curves of the true endmembers (EM) were not included. Each dataset is bounded by mixed EMs (solid colored curves) which are themselves mixtures of the true EMs. The data range in (a–c) shows the mixing degree of each dataset with respect to the true EMs; (d) the quantification of EM2 from EM-IRM unmixing of each dataset is plotted against the expected MTB contribution to bulk M_{rs} (colored lines with dots). It demonstrates that reconstructed concentrations of mixed EM2 significantly deviate from the expected concentration of the true MTB EM indicated by the gray line. If the relationship between mixed EMs and the true EMs are known, a correction can be made using Equation 5 so that concentrations of the true EMs can be calculated (thick colored lines).

endmembers. M defined by such data will be mixtures of true endmembers (see Figure 18 in Heslop, 2015), which is noted as M_{mix}. Consequently, resulting W_{mix} is biased from W_{true}.

The difference between W_{mix} and W_{true} depends on the actual data variability with respect to the full mixing space. Figure 7 illustrates this by unmixing three numerically synthesized datasets with different mixing degrees of two endmembers. The true endmembers are the MSR-1 and andesite endmembers used in Figure 5, but the IRM curves of the true endmembers are excluded from the datasets. Instead, each dataset in Figures 7a–7c is bounded by mixtures (EM1 and EM2 shown as colored curves), which are empirical endmembers used in EM-IRM unmixing. The relationships between the empirical and true endmembers are shown in the insets of Figures 7a–7c where "0" indicates pure andesite and "1" indicates pure MSR-1 endmember. It can be observed that the narrower the data range is compared to the full mixing range, the more biased the empirical endmembers (thick colored lines in Figures 7a–7c) are from the true endmembers. Concentration of EM2 (M_{rs_EM2}/M_{rs_bulk}) by EM-IRM unmixing of each dataset is shown against corresponding MSR-1 concentration ($M_{rs\_MSR\text{-}1}/M_{rs\_bulk}$) as lines with dots in Figure 7d. It is obvious that, even though the linearity is preserved, reconstructed concentrations of EM2 (thin colored lines with dots in Figure 7d) are different from the expected concentration of the MSR-1 endmember (gray line in Figure 7d). It can be found that the difference between the estimated EM2 concentration and the expected MSR-1 endmember becomes more pronounced as EM1 and EM2 become less distinctive (Figure 7d). For unmixing approaches based on NMF (Heslop & Dillon, 2007; Heslop & Roberts, 2012) and FORC-PCA (Harrison et al., 2018; Lascu et al., 2015), though endmembers can be chosen from ranges slightly beyond that defined by datasets, they are in general unlikely to be true endmembers. Nevertheless, if the quantitative relationship between reconstructed endmembers and true endmembers can be defined, contributions of

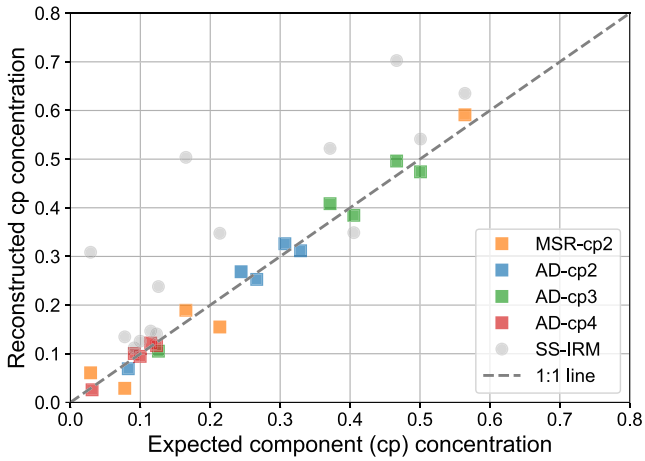

Figure 8. Results of hybrid unmixing. The estimated concentrations of some components of the mixtures closely trace the expected trend as indicated by the 1:1 line. Gray circles are the results of SS-IRM unmixing shown in Figure 4i.

reconstructed endmembers can be readily converted to that of the true members as follows. Under the assumption of a linear combination, true and reconstructed endmembers are expressed as

$$M_{\text{mix}} = HM_{\text{true}} + \boldsymbol{\varepsilon} \approx HM_{\text{true}}, \tag{4}$$

where M_{true} is the matrix of true endmembers and matrix H is the corresponding mixing ratios. Note that the numbers of true and reconstructed endmembers are not necessarily equal. If H and M_{true} are known, the datasets can be unmixed to the true endmembers using Equations 3 and 4:

$$D = W_{\text{mix}}M_{\text{mix}} + E \approx W_{\text{mix}}HM_{\text{true}} = W_{\text{true}}M_{\text{true}}. \tag{5}$$

Figure 7d shows the corrected estimates of the MSR-1 endmember (indicated by the thick lines superimposed on the gray line) using Equation 5.

4.4. Strategy for Unmixing Natural Samples

As stated above, EM-IRM unmixing is better at reconstructing the linear dependence within datasets, the level of unmixing will be superficial if the endmembers defined by a dataset are not sufficiently distinctive. On the other hand, even true endmembers of natural samples may consist of multiple components (e.g., Just et al., 2012). In order to unmix IRM curves to a lower level to infer mineralogical information, SS-IRM unmixing remains a powerful option. For example, previous studies (e.g., Huang et al., 2015; Just et al., 2012) further decompose reconstructed endmembers in order to understand their compositions. Here, we demonstrate that EM-IRM and SS-IRM unmixing methods can be quantitatively combined in order to maximize the potential of component analysis. For example, by combining the reconstructed concentrations of the mixtures samples based on both methods (Figures 4a, 4g, and 5) through Equation 5, we are able to better quantify the underlying components of the andesite and MSR-1 endmembers (Figure 8). Note that these components either cannot be identified by EM-IRM unmixing or are poorly reconstructed by SS-IRM unmixing (gray circles in Figure 8). With this hybrid unmixing approach, the estimates of MSR-cp2, AD-cp2, and AD-cp3 are successfully quantified. Also, the hybrid unmixing yields very close estimates for the putative hematite fractions (AD-cp4) even for sample Mix-E (indicated by the red square close to the origin of Figure 8), which accounts for only ~2.6% of its $M_{\text{rs\_bulk}}$ and was failed to be identified by SS-IRM unmixing. These results demonstrate the advantage of the hybrid approach over SS-IRM unmixing at reconstructing (1) components with high similarity and (2) components with extremely low contribution, owing to the fact that the hybrid approach avoid direct unmixing of less distinctive samples where SS-IRM unmixing is more susceptible to uncertainty (see section 4.2).

Using this strategy, experimental efforts can be prioritized to representative samples or endmembers. For example, SS-IRM unmixing and FORC analysis for weakly magnetized samples such as marine sediments are actually very demanding on data quality, which can be improved by stacking multiple measurements. While it is impractical to do so for all samples, it would be manageable for just representative samples.

In addition, our study shows that the unmixing results by EM-IRM unmixing and FORC-PCA are comparable. Considering the cost of time for FORC measurements, the results obtained by EM-IRM unmixing are actually impressive. FORC-PCA can be considered as an expensive alternative for the unmixing purpose. Nevertheless, the advantage of FORCs-related analysis outstands for understanding magnetizing processes and assessing domain states of magnetic materials.

5. Conclusions

Despite the fact that component analysis of isothermal remanent magnetization (IRM) curves is widely applied to natural samples, the reliability of unmixing results remain to be verified due to lacking independent verification. We designed experiments using mixture samples consisting of two endmembers to benchmark the unmixing results based on IRM curves. The single-sample-based IRM (SS-IRM) unmixing

approach did not generate reliable estimates. It is found that results are more likely to be compromised when reconstructed components have highly overlapping coercivity distributions and/or weak magnetization. In these circumstances, this method can be very sensitive to factors such as the choice of model distribution and measurement noise.

Compared to SS-IRM unmixing, an ad-hoc endmember-based IRM (EM-IRM) unmixing approach yielded significant improvement, suggesting that endmember-based component analysis is a more robust approach to unmixing a collection of IRM curves. The level of unmixing, however, depends on the endmembers defined by investigated datasets. It means that EM mixing coefficients (W) will vary with the mixing degree of the endmembers. We demonstrated by a two-endmember system that EM-IRM unmixing can adequately reconstruct W when true endmembers can be reasonably identified. On the other hand, if endmembers are highly mixed, which could be indicated by narrow variability of the IRM dataset under investigation, endmember-based methods will result in W of mixed endmembers rather than true endmembers. For the purpose of further unmixing endmembers, SS-IRM unmixing and FORC-type diagrams are helpful options. Once endmembers have been decomposed into underlying components using, for example, SS-IRM unmixing, W can be readily converted to reflect mixing ratios of the corresponding components to facilitate the interpretation of data and associated geological processes.

Data Availability Statement

The IRM data analyzed in this study can be found at https://figshare.com/s/810add3e05f7cb5c8762, and the associated Python codes can be found at https://figshare.com/s/356ad77f64217292c1d0.

Acknowledgments

We thank Xu Tang at the Electron Microscopy Laboratory, IGGCAS, for help in SAED experiment. The authors thank Wei Lin for valuable discussions and Shuangchi Liu for experimental help. The work was supported by the National Natural Science Foundation of China (41621004 and 41904070) and the Strategic Priority Research Program of Chinese Academy of Sciences (XDB18010000). This study was also supported by the National Institute of Polar Research (NIPR) through Advanced Project (KP-7 and KP306) and JSPS KAKENHI grants (15K13581, 16H04068, 17H06321, and 18K13638). X. Z. acknowledges the Australian Research Council Discovery Projects DP200100765 and the National Natural Science Foundation of China (grant 41920104009) for financial supports. We are grateful to Tilo von Dobeneck, Thomas Berndt, Mark Dekkers and Isabelle Manighetti for their thoughtful comments that improved our manuscript.

References

Akaike, H. (1998). Information theory and an extension of the maximum likelihood principle. In E. Parzen, K. Tanabe, G. Kitagawa (Eds.), *Selected papers of Hirotugu Akaike*, *Springer Series in Statistics (Perspectives in Statistics)* (pp. 199–213). New York, NY: Springer. https://doi.org/10.1007/978-1-4612-1694-0_15

Burnham, K. P., & Anderson, D. R. (2002). Information and Likelihood Theory: A Basis for Model Selection and Inference. *Model selection and multimodel inference: A practical information-theoretic approach* (2nd ed.). New York: Springer-Verlag. https://doi.org/10.1007/978-0-387-22456-5_2

Channell, J. E. T., Hodell, D. A., Margari, V., Skinner, L. C., Tzedakis, P. C., & Kesler, M. S. (2013). Biogenic magnetite, detrital hematite, and relative paleointensity in Quaternary sediments from the Southwest Iberian Margin. *Earth and Planetary Science Letters*, *376*, 99–109. https://doi.org/10.1016/j.epsl.2013.06.026

Chen, A. P., Berounsky, V. M., Chan, M. K., Blackford, M. G., Cady, C., Moskowitz, B. M., et al. (2014). Magnetic properties of uncultivated magnetotactic bacteria and their contribution to a stratified estuary iron cycle. *Nature Communications*, *5*(1), 4797. https://doi.org/10.1038/ncomms5797

Day, R., Fuller, M., & Schmidt, V. A. (1977). Hysteresis properties of titanomagnetites: Grain-size and compositional dependence. *Physics of the Earth and Planetary Interiors*, *13*(4), 260–267. https://doi.org/10.1016/0031-9201(77)90108-X

Dekkers, M. J. (2012). End-member modelling as an aid to diagnose remagnetization: A brief review. *Geological Society, London, Special Publications*, *371*(1), 253–269. https://doi.org/10.1144/SP371.12

Dunlop, D. J. (1973). Superparamagnetic and single-domain threshold sizes in magnetite. *Journal of Geophysical Research*, *78*(11), 1780–1793. https://doi.org/10.1029/JB078i011p01780

Dunlop, D. J. (2002). Theory and application of the Day plot (M_{rs}/M_s versus H_{cr}/H_c) 2. Application to data for rocks, sediments, and soils. *Journal of Geophysical Research*, *107*(B3), EPM 5–1–EPM 5–15. https://doi.org/10.1029/2001JB000487

Dunlop, D. J., & Bina, M. M. (1977). The coercive force spectrum of magnetite at high temperatures: Evidence for thermal activation below the blocking temperature. *Geophysical Journal International*, *51*(1), 121–147. https://doi.org/10.1111/j.1365-246X.1977.tb04193.x

Egli, R. (2003). Analysis of the field dependence of remanent magnetization curves. *Journal of Geophysical Research*, *108*(B2), 2081. https://doi.org/10.1029/2002JB002023

Egli, R. (2004a). Characterization of individual rock magnetic components by analysis of remanence curves, 1. Unmixing natural sediments. *Studia Geophysica et Geodaetica*, *48*(2), 391–446. https://doi.org/10.1023/B:SGEG.0000020839.45304.6d

Egli, R. (2004b). Characterization of individual rock magnetic components by analysis of remanence curves: 2. Fundamental properties of coercivity distributions. *Physics and Chemistry of the Earth, Parts A/B/C*, *29*(13–14), 851–867. https://doi.org/10.1016/j.pce.2004.04.001

Egli, R., Chen, A. P., Winklhofer, M., Kodama, K. P., & Horng, C. (2010). Detection of noninteracting single domain particles using first-order reversal curve diagrams. *Geochemistry, Geophysics, Geosystems*, *11*, Q01Z11. https://doi.org/10.1029/2009GC002916

Fabian, K., Shcherbakov, V. P., Kosareva, L., & Nourgaliev, D. (2016). Physical interpretation of isothermal remanent magnetization endmembers: New insights into the environmental history of Lake Hovsgul, Mongolia. *Geochemistry, Geophysics, Geosystems*, *17*, 4669–4683. https://doi.org/10.1002/2016GC006506

Frankel, R. B., & Blakemore, R. P. (1989). Magnetite and magnetotaxis in microorganisms. *Bioelectromagnetics*, *10*(3), 223–237. https://doi.org/10.1002/bem.2250100303

Harrison, R. J., & Feinberg, J. M. (2008). FORCinel: An improved algorithm for calculating first-order reversal curve distributions using locally weighted regression smoothing. *Geochemistry, Geophysics, Geosystems*, *9*, Q05016. https://doi.org/10.1029/2008GC001987

Harrison, R. J., Muraszko, J., Heslop, D., Lascu, I., Muxworthy, A. R., & Roberts, A. P. (2018). An improved algorithm for unmixing first-order reversal curve diagrams using principal component analysis. *Geochemistry, Geophysics, Geosystems*, *19*, 1595–1610. https://doi.org/10.1029/2018GC007511

Heslop, D. (2015). Numerical strategies for magnetic mineral unmixing. *Earth-Science Reviews*, *150*, 256–284. https://doi.org/10.1016/j.earscirev.2015.07.007

Heslop, D., Dekkers, M. J., Kruiver, P. P., & Van Oorschot, I. H. (2002). Analysis of isothermal remanent magnetization acquisition curves using the expectation-maximization algorithm. *Geophysical Journal International*, *148*(1), 58–64. https://doi.org/10.1046/j.0956-540x.2001.01558.x

Heslop, D., & Dillon, M. (2007). Unmixing magnetic remanence curves without a priori knowledge. *Geophysical Journal International*, *170*(2), 556–566. https://doi.org/10.1111/j.1365-246X.2007.03432.x

Heslop, D., & Roberts, A. P. (2012). A method for unmixing magnetic hysteresis loops. *Journal of Geophysical Research*, *117*, B03103. https://doi.org/10.1029/2011JB008859

Huang, W., Dupont-Nivet, G., Lippert, P. C., Van Hinsbergen, D. J., Dekkers, M. J., Guo, Z., et al. (2015). Can a primary remanence be retrieved from partially remagnetized Eocence volcanic rocks in the Nanmulin Basin (southern Tibet) to date the India-Asia collision? *Journal of Geophysical Research: Solid Earth*, *120*, 42–66. https://doi.org/10.1002/2014JB011599

Just, J., Dekkers, M. J., von Dobeneck, T., van Hoesel, A., & Bickert, T. (2012). Signatures and significance of aeolian, fluvial, bacterial and diagenetic magnetic mineral fractions in Late Quaternary marine sediments off Gambia, NW Africa. *Geochemistry, Geophysics, Geosystems*, *13*, Q0AO02. https://doi.org/10.1029/2012GC004146

King, J. W., & Channell, J. E. (1991). Sedimentary magnetism, environmental magnetism, and magnetostratigraphy. *Reviews of Geophysics*, *29*(S1), 358–370. https://doi.org/10.1002/rog.1991.29.s1.358

Kruiver, P. P., Dekkers, M. J., & Heslop, D. (2001). Quantification of magnetic coercivity components by the analysis of acquisition curves of isothermal remanent magnetisation. *Earth and Planetary Science Letters*, *189*(3–4), 269–276. https://doi.org/10.1016/S0012-821X(01)00367-3

Larrasoaña, J. C., Roberts, A. P., Chang, L., Schellenberg, S. A., Gerald, J. D. F., Norris, R. D., & Zachos, J. C. (2012). Magnetotactic bacterial response to Antarctic dust supply during the Palaeocene–Eocene thermal maximum. *Earth and Planetary Science Letters*, *333–334*, 122–133. https://doi.org/10.1016/j.epsl.2012.04.003

Lascu, I., Banerjee, S. K., & Berquo, T. S. (2010). Quantifying the concentration of ferrimagnetic particles in sediments using rock magnetic methods. *Geochemistry, Geophysics, Geosystems*, *11*, Q08Z19. https://doi.org/10.1029/2010GC003182

Lascu, I., Harrison, R. J., Li, Y., Muraszko, J., Channell, J. E., Piotrowski, A. M., & Hodell, D. A. (2015). Magnetic unmixing of first-order reversal curve diagrams using principal component analysis. *Geochemistry, Geophysics, Geosystems*, *16*, 2900–2915. https://doi.org/10.1002/2015GC005909

Li, J., Pan, Y., Liu, Q., Yu-Zhang, K., Menguy, N., Che, R., et al. (2010). Biomineralization, crystallography and magnetic properties of bullet-shaped magnetite magnetosomes in giant rod magnetotactic bacteria. *Earth and Planetary Science Letters*, *293*(3–4), 368–376. https://doi.org/10.1016/j.epsl.2010.03.007

Lin, W., Bazylinski, D. A., Xiao, T., Wu, L., & Pan, Y. (2014). Life with compass: Diversity and biogeography of magnetotactic bacteria. *Environmental Microbiology*, *16*(9), 2646–2658. https://doi.org/10.1111/1462-2920.12313

Lin, W., Pan, Y., & Bazylinski, D. A. (2017). Diversity and ecology of and biomineralization by magnetotactic bacteria. *Environmental Microbiology Reports*, *9*(4), 345–356. https://doi.org/10.1111/1758-2229.12550

Liu, Q., Roberts, A. P., Larrasoana, J. C., Banerjee, S. K., Guyodo, Y., Tauxe, L., & Oldfield, F. (2012). Environmental magnetism: Principles and applications. *Reviews of Geophysics*, *50*, RG4002. https://doi.org/10.1029/2012RG000393

Lowrie, W. (1990). Identification of ferromagnetic minerals in a rock by coercivity and unblocking temperature properties. *Geophysical Research Letters*, *17*(2), 159–162. https://doi.org/10.1029/GL017i002p00159

Mao, X., Egli, R., Petersen, N., Hanzlik, M., & Zhao, X. (2014). Magnetotaxis and acquisition of detrital remanent magnetization by magnetotactic bacteria in natural sediment: First experimental results and theory. *Geochemistry, Geophysics, Geosystems*, *15*, 255–283. https://doi.org/10.1002/2013GC005034

Maxbauer, D. P., Feinberg, J. M., & Fox, D. L. (2016). MAX UnMix: A web application for unmixing magnetic coercivity distributions. *Computers & Geosciences*, *95*, 140–145. https://doi.org/10.1016/j.cageo.2016.07.009

McNab, T. K., Fox, R. A., & Boyle, A. J. (1968). Some magnetic properties of magnetite (Fe_3O_4) microcrystals. *Journal of Applied Physics*, *39*(12), 5703–5711. https://doi.org/10.1063/1.1656035

Moskowitz, B. M., Frankel, R. B., & Bazylinski, D. A. (1993). Rock magnetic criteria for the detection of biogenic magnetite. *Earth and Planetary Science Letters*, *120*(3–4), 283–300. https://doi.org/10.1016/0012-821X(93)90245-5

Newell, A. J. (2005). A high-precision model of first-order reversal curve (FORC) functions for single-domain ferromagnets with uniaxial anisotropy. *Geochemistry, Geophysics, Geosystems*, *6*, Q05010. https://doi.org/10.1029/2004GC000877

Pan, Y., Petersen, N., Davila, A. F., Zhang, L., Winklhofer, M., Liu, Q., et al. (2005). The detection of bacterial magnetite in recent sediments of Lake Chiemsee (southern Germany). *Earth and Planetary Science Letters*, *232*(1–2), 109–123. https://doi.org/10.1016/j.epsl.2005.01.006

Pan, Y., Petersen, N., Winklhofer, M., Davila, A. F., Liu, Q., Frederichs, T., et al. (2005). Rock magnetic properties of uncultured magnetotactic bacteria. *Earth and Planetary Science Letters*, *237*(3–4), 311–325. https://doi.org/10.1016/j.epsl.2005.06.029

Paterson, G. A., Wang, Y., & Pan, Y. (2013). The fidelity of paleomagnetic records carried by magnetosome chains. *Earth and Planetary Science Letters*, *383*, 82–91. https://doi.org/10.1016/j.epsl.2013.09.031

Paterson, G. A., Zhao, X., Jackson, M., & Heslop, D. (2018). Measuring, processing, and analyzing hysteresis data. *Geochemistry, Geophysics, Geosystems*, *19*, 1925–1945. https://doi.org/10.1029/2018GC007620

Pei, J., Sun, Z., Liu, J., Liu, J., Wang, X., Yang, Z., et al. (2011). A paleomagnetic study from the Late Jurassic volcanics (155 Ma), North China: Implications for the width of Mongol–Okhotsk Ocean. *Tectonophysics*, *510*(3–4), 370–380. https://doi.org/10.1016/j.tecto.2011.08.008

Pike, C. R., Roberts, A. P., & Verosub, K. L. (1999). Characterizing interactions in fine magnetic particle systems using first order reversal curves. *Journal of Applied Physics*, *85*(9), 6660–6667. https://doi.org/10.1063/1.370176

Roberts, A. P., Chang, L., Heslop, D., Florindo, F., & Larrasoaña, J. C. (2012). Searching for single domain magnetite in the "pseudo-single-domain" sedimentary haystack: Implications of biogenic magnetite preservation for sediment magnetism and relative paleointensity determinations. *Journal of Geophysical Research*, *117*, B08104. https://doi.org/10.1029/2012JB009412

Roberts, A. P., Florindo, F., Villa, G., Chang, L., Jovane, L., Bohaty, S. M., et al. (2011). Magnetotactic bacterial abundance in pelagic marine environments is limited by organic carbon flux and availability of dissolved iron. *Earth and Planetary Science Letters*, *310*(3–4), 441–452. https://doi.org/10.1016/j.epsl.2011.08.011

Roberts, A. P., Liu, Q., Rowan, C. J., Chang, L., Carvallo, C., Torrent, J., & Horng, C. S. (2006). Characterization of hematite (α-Fe_2O_3), goethite (α-FeOOH), greigite (Fe_3S_4), and pyrrhotite (Fe_7S_8) using first-order reversal curve diagrams. *Journal of Geophysical Research*, *111*, B12S35. https://doi.org/10.1029/2006JB004715

Roberts, A. P., Pike, C. R., & Verosub, K. L. (2000). First-order reversal curve diagrams: A new tool for characterizing the magnetic properties of natural samples. *Journal of Geophysical Research*, *105*(B12), 28,461–28,475. https://doi.org/10.1029/2000JB900326

Roberts, A. P., Tauxe, L., Heslop, D., Zhao, X., & Jiang, Z. (2018). A critical appraisal of the "Day" diagram. *Journal of Geophysical Research: Solid Earth*, *123*, 2618–2644. https://doi.org/10.1002/2017JB015247

Robertson, D. J., & France, D. E. (1994). Discrimination of remanence-carrying minerals in mixtures, using isothermal remanent magnetisation acquisition curves. *Physics of the Earth and Planetary Interiors*, *82*(3–4), 223–234. https://doi.org/10.1016/0031-9201(94)90074-4

Tauxe, L., Mullender, T. A. T., & Pick, T. (1996). Potbellies, wasp-waists, and superparamagnetism in magnetic hysteresis. *Journal of Geophysical Research*, *101*(B1), 571–583. https://doi.org/10.1029/95JB03041

Usui, Y., Yamazaki, T., & Saitoh, M. (2017). Changing abundance of magnetofossil morphologies in pelagic red clay around Minamitorishima, Western North Pacific. *Geochemistry, Geophysics, Geosystems*, *18*, 4558–4572. https://doi.org/10.1002/2017GC007127

Weltje, G. J. (1997). End-member modeling of compositional data: Numerical-statistical algorithms for solving the explicit mixing problem. *Mathematical Geology*, *29*(4), 503–549. https://doi.org/10.1007/BF02775085

Zhang, T., & Pan, Y. (2018). Constraining the magnetic properties of ultrafine-and fine-grained biogenic magnetite. *Earth, Planets and Space*, *70*(1), 206. https://doi.org/10.1186/s40623-018-0978-2

Zhao, X., Egli, R., Gilder, S. A., & Müller, S. (2016). Microbially assisted recording of the Earth's magnetic field in sediment. *Nature Communications*, *7*(1), 10673. https://doi.org/10.1038/ncomms10673

Zhao, X., Fujii, M., Suganuma, Y., Zhao, X., & Jiang, Z. (2018). Applying the Burr type XII distribution to decompose remanent magnetization curves. *Journal of Geophysical Research: Solid Earth*, *123*, 8298–8311. https://doi.org/10.1029/2018JB016082

Zhao, X., Heslop, D., & Roberts, A. P. (2015). A protocol for variable-resolution first-order reversal curve measurements. *Geochemistry, Geophysics, Geosystems*, *16*, 1364–1377. https://doi.org/10.1002/2014GC005680

Zhao, X., Roberts, A. P., Heslop, D., Paterson, G. A., Li, Y., & Li, J. (2017). Magnetic domain state diagnosis using hysteresis reversal curves. *Journal of Geophysical Research: Solid Earth*, *122*, 4767–4789. https://doi.org/10.1002/2016JB013683